Published in final edited form as:
Lab Chip. 2008 January ; 8(1): 125–133. doi:10.1039/b713626a.

Optical sectioning for microfluidics: secondary flow and mixing in a meandering microchannel†

Yeh-Chan Ahn, **Woonggyu Jung**, and **Zhongping Chen***
Beckman Laser Institute and Department of Biomedical Engineering, University of California, Irvine, Irvine, CA, USA

Abstract

Secondary flow plays a critical function in a microchannel, such as a micromixer, because it can enhance heat and mass transfer. However, there is no experimental method to visualize the secondary flow and the associated mixing pattern in a microchannel because of difficulties in high-resolution, non-invasive, cross-sectional imaging. Here, we simultaneously imaged and quantified the secondary flow and pattern of two-liquid mixing inside a meandering square microchannel with spectral-domain Doppler optical coherence tomography. We observed an increase in the efficiency of two-liquid mixing when air was injected to produce a bubble-train flow and identified the three-dimensional enhancement mechanism behind the complex mixing phenomena. An alternating pair of counter-rotating and toroidal vortices cooperated to enhance two-liquid mixing.

Introduction

A Reynolds number of the primary flow in a microchannel is usually less than 100 and one cannot expect turbulent mixing. In order to enhance mixing efficiency, time-periodic or geometrical-periodic perturbations have been suggested.[1] All of them result in an increased complexity in the secondary flow. However, there is no experimental method to visualize the secondary flow and the associated mixing pattern in a microchannel because of difficulties in high-resolution, non-invasive, cross-sectional imaging.

In this article, we report the observation of secondary flow and convective two-liquid mixing in a meandering microchannel using spectral-domain Doppler optical coherence tomography (SDDOCT).[2–4] We observed an increased efficiency of mixing in liquid slugs when air was injected to produce a bubble-train flow. SDDOCT is an emerging imaging modality that has high-speed, high-resolution, non-invasive, cross-sectional imaging capability. Since SDDOCT allows simultaneous real-time visualization of sample structure and flow, it is often compared to clinical ultrasound. However, the spatial resolution of clinical ultrasound is limited to approximately 100 mm due to the relatively long wavelength of acoustic waves. SDDOCT takes advantage of the short coherence length of broadband light sources in order to achieve cross-sectional images with micrometer (2–10 μm) scale resolution. SDDOCT is also superior to ultrasound in that SDDOCT is operated in non-contact-mode. Because of the aforementioned merits, SDDOCT has received a great deal of attention in the fields of biology and medicine. However, SDDOCT has seldom been applied to microscale flow and mixing visualizations.

†Electronic supplementary information (ESI) available: Theory of SDDOCT, supplementary video 1 (volume-rendered mixing pattern), 2 (enhanced mixing pattern 1 in bubble-train flow), 3 (enhanced mixing pattern 2 in bubble-train flow), and 4 (enhanced mixing pattern 3 in bubble-train flow). See DOI: 10.1039/b713626a

ahny@uci.edu; z2chen@uci.edu; Fax: +1-949-824-8413; Tel: +1-949-824-1247.

When SDDOCT is compared to other techniques for microscale visualization, the uniqueness of SDDOCT can be summarized in Table 1. Fluorescence microscopy (FM) and confocal laser scanning microscopy (CLSM) provide better spatial resolution but cannot measure flow and mixing simultaneously, need transparent liquids and conduits, and give an *en face* image rather than a cross-sectional image. In contrast to FM, CLSM is able to image different depths but its accessible depth is limited to 0.5 mm.5 Micro particle imaging velocimetry (μPIV) has been a useful tool for microfluidics, but it is difficult to measure out-of-plane velocity which is parallel to line-of-sight6 and is not capable of real-time imaging. A multi-beam SDDOCT can quantify a velocity vector with three components without complex post-processing.7 In order to enhance spatial resolution of clinical ultrasound, ultrasound biomicroscopy (UBM) with a high-frequency (100–200 MHz) transducer was demonstrated and achieved 15 μm spatial resolution.8 However, UBM is expensive, has to sacrifice imaging depth in order to enhance spatial resolution, and still needs contact-mode. X-Ray is another alternative for microscale visualization.9›10 It works with opaque conduits and provides high spatial resolution. Imaging speed, however, is slow, and it needs synchrotron radiation.

Since its first demonstration,[11] the secondary flow inside a curved channel[12–18] has received much attention because it is found in many areas from heat exchangers to human arterial systems.[19,20] All previous experimental works were done with large pipes and utilized laser Doppler anemometry[21,22] or tracers,[11,19,20,23,24] like dye, hydrogen bubble, or powder, to explore the secondary flow. Recently, mixing by chaotic advection was demonstrated in droplets moving through a meandering microchannel.[25] The droplets with two aqueous reagents were separated by oil. It was hypothesized that the reagents in the droplets experienced the baker's transformation: the reagents were folded and stretched by the recirculating flow in the straight portion of the microchannel and reoriented as the reagents moved around a turn. However, it was difficult to clearly visualize mixing patterns that corresponded to the baker's transformation because the microscope-based imaging system provided an *en face* image integrated along line-of-sight and could not image three-dimensional mixing patterns. This was the reason that the authors gave only a two-dimensional description in the *en face* plane. Here, we emphasize SDDOCT's capability of three-dimensional tomographic imaging and measurement of out-of-plane velocity component to show a full mechanism behind complex mixing phenomena.

In the Theory section, we will show the mathematical details about the interaction between light and moving particles based on a Michelson interferometer. We will present experimental conditions and procedures including how to make a volume image in the Methods section. In the Results and discussion section, we will show velocity images for the secondary flow and mixing pattern images with/without air injection which enhances two-liquid mixing. We will discuss three-dimensional enhancement mechanism before we conclude.

Theory

While the theoretical background of optical coherence tomography in the spectral-domain has been reported,[26–28] the Doppler effect has not been rigorously derived yet. In this section, we will summarize how the Doppler effect can be formulated for SDDOCT (see ESI† for its detailed derivation).

SDDOCT is a fusion of laser Doppler velocimetry and optical coherence tomography based on a Michelson interferometer shown in Fig. 1. Four arms around a 50 : 50 beam splitter in the Michelson interferometer are assigned by a low-coherence light source at the source arm, a spectrometer with a line array of detectors and a diffraction grating at the detector arm, an immobilized mirror at the reference arm, and a two-axis scanner and a sample with moving scatterers at the sample arm. Reflected lights from the immobilized mirror and each scattering

particle in the sample make a signal in the spectral-domain which is detected by the spectrometer.

In order to describe the principle of SDDOCT, let us consider a steady-state velocity field of the moving scatterers, $\mathbf{V}(\mathbf{X}) = (v_X, v_Y, v_Z)$ as a function of the position vector $\mathbf{X} = (X, Y, Z)$. The coordinates X, Y, and Z are attached on the microchannel shown in Fig. 1 and the XZ-plane is the top surface and the Y-coordinate is the depthwise direction of the microchannel. Let us define another set of coordinates, x, y, z, attached on the sample arm. Then, the description of the velocity field is $\mathbf{V}(\mathbf{x}) = (v_x, v_y, v_z)$ as a function of position vector $\mathbf{x} = (x, y, z)$. Let us have the y-coordinate coincide with the incident light to the microchannel. In order to measure v_Y with SDDOCT, we keep the incident light aligned to the Y-direction during two-axis scanning of the light in the x- and z-directions. Once a line field of $v_y(y)$ at a fixed position of (x, z) is measured, the scanner moves the light to another position of (x, z) to get a three-dimensional velocity field of $v_y(x, y, z)$. We, hereafter, describe how the line field is measured.

The instantaneous positions of moving scatterers in the y-coordinate are described as $y = y_0 + v_y(y_0)t$ for a sufficiently short time t where y_0 denotes initial positions. Now let us consider an input analytic signal $U_{\text{in}}(\omega, t)$ to the interferometer:

$$U_{\text{in}}(\omega, t) = s(\omega)\exp[-i(\omega t - \varphi)], \tag{1}$$

where $s(\omega)$ is amplitude spectrum of the light source, ω is frequency, and φ is phase accumulated throughout the interferometer. Since the interferometer only measures the relative phase between two optical paths, the phase of the input analytic signal U_{in} is chosen as a reference and the input analytic signal is written as $U_{\text{in}}(\omega,t) = s(\omega)\exp(-i\omega t)$. Then, the output analytic signal U_{out} is the sum of analytic signals at the reference $U_{\text{r}}(\omega,t)$ and sample arms $U_{\text{s}}(\omega,t)$ and a frequency response function $H(\omega,t)$ of a sample can be written as:

$$H(\omega, t) = \int_0^\infty a(y_0)\exp\left[-i\omega\left\{\left(\frac{1 - n_{\text{s}}v_y/c}{1+n_{\text{s}}v_y/c} - 1\right)t - \frac{2n_{\text{s}}(l_{\text{s}}+y_0)/c}{1+n_{\text{s}}v_y/c}\right\}\right]\mathrm{d}y_0, \tag{2}$$

where $a(y_0)$ is the initial distribution of backscattering amplitude, n_{s} is refractive index of the sample arm, c is the speed of light in free space, and l_{s} is the physical length between the beam splitter and the origin of the y-coordinate. The frequency response function provides the input analytic signal with time delay and compression factors. The time delay factor comes from the path length delay and the compression factor from the Doppler effect. In another point of view, the frequency response function represents instantaneous phase accumulation by the multiple optical paths within the sample and, therefore, is a sum of many elementary waves reflected from moving scatterers with different initial depths of $l_{\text{s}} + y_0$.

Now we adjust the physical length of the reference arm l_{r} to satisfy $n_{\text{r}}l_{\text{r}} = n_{\text{s}}l_{\text{s}}$. Once the spectrometer records the intensity I of the output analytic signal as a function of time t and wavenumber k $(= \omega/c)$ in free space, we take the inverse Fourier transform of the intensity from the k- to the $2n_{\text{s}}y_0$-domain (*i.e.* the optical double path length domain which will be denoted as η_0-domain) to get a final result:

$$\Im^{-1}[I(k,t)] = \frac{1}{4}\Im^{-1}[S(k)] + \frac{1}{8n_{\text{s}}}\Im^{-1}[S(k)] \otimes \left[\tilde{b}\left(\frac{\eta_0}{2n_{\text{s}}}\right)\exp(i2k_0n_{\text{s}}v_yt)\right] + \text{sample}-\text{intensityterm}, \tag{3}$$

where k_0 and $S(k)$ are the center wavenumber and the intensity spectrum of the light source, respectively, $\Im^{-1}$ and $\otimes$ denote inverse Fourier transform and convolution operator defined in the η_0-domain:

$$\Im^{-1}(F(k))=\frac{1}{2\pi}\int_{-\infty}^{\infty}F(k)\exp[-ik\eta_0]\mathrm{d}k, \tag{4}$$

$$(f\otimes g)(\eta_0)=\int_{-\infty}^{\infty}f(\eta_0')g(\eta_0'+\eta_0)\,\mathrm{d}\eta_0', \tag{5}$$

and $\tilde{b}(\eta_0/2n_s)$ is an even function defined as

$$\tilde{b}\left(\frac{\eta_0}{2n_s}\right)=\begin{cases} b(\eta_0/2n_s) \\ b(-\eta_0/2n_s) \end{cases}=\begin{cases} a(\eta_0/2n_s)\mathrm{sinc}(k_0n_sv_y(\eta_0/2n_s)\tau) & \text{if } \eta_0\geq 0 \\ a(-\eta_0/2n_s)\mathrm{sinc}(k_0n_sv_y(-\eta_0/2n_s)\tau) & \text{if } \eta_0<0 \end{cases}. \tag{6}$$

Here, τ is the integration time of the spectrometer.

The first term in eqn (3) can be pre-calibrated, and the third is negligible for a highly scattering sample.[26] The second term is our target signal and is referred to as the cross-interference term. The magnitude of the second term gives a structural image and the phase, a velocity image. Suppose that the light source has a Gaussian power spectral density with a center wavenumber k_0 and a full-width-half-maximum (FWHM) spectral width Δk in wavenumbers. The inverse Fourier transform of $S(k)$ with a broad bandwidth gives a narrow Gaussian distribution where the FWHM is $8\ln 2/\Delta k$ in the η_0-domain. If we have a stationary mirror as a sample, the structural image is the convolution of a delta function and $\Im^{-1}[S(k)]$ with a FWHM depth resolution of $4\ln 2/n_s\Delta k$ in the y_0-domain. If the mirror is moving with v_y, a motion artifact comes in because of the finite integration time τ and degrades the spatial resolution. In fact, the degradation can be explained by the convolution of the stationary image with a rect function, that is the inverse Fourier transform of the sinc function.[28] In order to get the line field of $v_y(y_0)$, we need two consecutive exposures of the spectrometer at time t and $t + T$ at a fixed position of (x, z). This gives two complex signals of $\Im^{-1}[I(k, t)]$ and $\Im^{-1}[I(k, t + T)]$. The ensemble average of phase difference between the complex signals can be related to the line field of velocity:

$$\overline{\Delta\phi}(y_0)=2k_0n_sv_y(y_0)T. \tag{7}$$

Since the ensemble average of the phase difference ranges from $-\pi$ to π, the detectable velocity range of v_y is from $-\lambda_0/4n_sT$ to $\lambda_0/4n_sT$ where λ_0 is the center wavelength. Any velocity outside this range will cause an aliasing effect. A phase unwrapping technique[29] using flow continuity can further increase this limitation by a factor of 4. Therefore, the time interval T should fall in the range of $\tau < T < \lambda_0/n_sv_y^{\max}$ where $v_y^{\max}$ is the maximum velocity.

Typical values of the parameters used in this study is as follows: τ = 24.4 μs, T = 129.6 μs, λ_0 = 1310 nm, $\Delta k = 0.33\ \mu\mathrm{m}^{-1}$, $4\ln 2/n_s\Delta k$ (depth resolution) = 6.3 μm, and the ensemble number N for the averaging of the phase difference = 4. This technique to measure the line velocity field can be applied to a transient flow if NT is reasonably smaller than the characteristic time scale of the transient flow. By adjusting the orientation of the incident light relative to the sample, we can basically measure any component of velocity vector for a steady-state flow.

We, however, are focusing on the out-of-plane velocity v_Y in this study, not only to emphasize the SDDOCT's capability but also to address the secondary flow.

Methods

Experimental details

A meandering square microchannel (SMS0104; thinXXS Microtechnology AG, Mainz, Germany) made of cyclo-olefin copolymer is shown in Fig. 2(b). It has a Y branch at the beginning, and the dimension of cross-section between confluence and outlet is 600 μm × 600 μm. The radius of curvature R has a minimum of 1.7 mm. Four groups of experiments were conducted as summarized in Table 2. First, there was a single-phase liquid flow experiment where a 2.5% aqueous suspension of polystyrene beads (0.2 μm in diameter and 1.05 g cm^{-3} in density) was injected into inlets 1 and 2 of the Y branch. The secondary flow was visualized with different flow rates (0.2, 0.4, and 0.6 ml min^{-1} per inlet). Second, there was a two-liquid mixing experiment where deionized water and a 2.5% aqueous suspension of polystyrene beads were injected into inlets 1 and 2, respectively. The mixing pattern was observed with different flow rates (0.2 and 0.6 ml min^{-1} per inlet). Third, there was a gas–liquid mixing experiment where a 2.5% aqueous suspension of polystyrene beads and air were injected into inlet 1 with a flow rate of 0.25 ml min^{-1} and inlet 2 with a flow rate of 0.08 ml min^{-1}. The enhancement of the secondary flow was imaged. Four, a two-liquid mixing enhanced by gas injection was visualized. A 2.5% aqueous suspension of polystyrene beads and the deionized water were injected into inlets 1−1 and 1–2, respectively, with a flow rate of 0.125 ml min^{-1} for each and the air into inlet 2 with a flow rate of 0.08 ml min^{-1}. Since the density of polystyrene beads is almost the same as that of water, the beads follow the mean liquid movement faithfully. The average distance between beads is sufficiently smaller than the current imaging resolution with a particle concentration of 2.5%. Hence, the resolution is not limited by the particle number density. The ensemble average of the phase difference addressed in the previous section reduces the effect of Brownian motion which is not negligible with a small bead diameter. All fluids were injected by dual-syringe pumps (11 Plus; Harvard Apparatus, Holliston, MA) with ±0.5% flow rate accuracy.

Producing method of images

SDDOCT measures the y-component of the velocity field $v_y(x, y, z)$ which is the particle velocity projected on the incident light. When the incident light is normal at the top or bottom surface of the meandering microchannel, the detected velocity does not include the primary flow. However, high backscatterings from the top and bottom surfaces give rise to saturation of the detector in the spectrometer so that the microchannel is slightly tilted with respect to the X-axis by $\alpha = -1.5°$ from the normal illumination [see Fig. 2(a)]. If the normal illumination has a relationship between two frames: $x = X$, $y = Y$, and $z = Z$, the new relationship due to the tilting is $x = X$, $y = Y\cos\alpha - Z\sin\alpha$, and $z = Y\sin\alpha + Z\cos\alpha$. Because of the −1.5° tilting, the effect of the primary flow is included except when the primary flow at certain positions [for example, the positions marked by ● in Fig. 2(b)] is parallel to the X-axis (note that the incident light or y-axis is normal to the primary flow parallel to the X-axis).

Four camera exposures were averaged to make an A-scan (a scan along the y-axis) and 4000 exposures for the B-scan (a scan along the x-axis) constituted a cross-sectional image. Cross-sectional images were taken every 5 μm during the C-scan (a scan along the z-axis) and a total of 1200 images was rendered to construct a tilted volume image. The physical size of a voxel was 5 μm (x) × 6.3 μm (y) × 5 μm (z). Once we obtained the tilted volume image in the xyz frame, we transformed the xyz frame to the XYZ frame and sectioned the volume image with the XY-, YZ-, and XZ-planes to generate the images in Fig. 3 and Fig. 4.

Results and discussion

This study is composed of four experiments with a meandering square microchannel. The first experiment was intended to measure the liquid velocity within the area of interest in Fig. 2(b). The area was scanned by the two-axis scanner shown in Fig. 2(a). The *y*-component of the velocity field $v_y(X, Y, Z)$ is shown in Fig. 3.

Each horizontal row in Fig. 3 has a different flow rate shown in Table 2. The Reynolds number *Re* is defined by $Re = VW/v$ for each row was 11, 22, and 33, respectively, where *V* is the cross-sectional average of the primary velocity, *W* is the channel width, and *v* is the kinematic viscosity. Top views (the *XZ*-plane) from the second to the fourth column in Fig. 3 were reconstructed from volume images. The second column [Fig. 3(f), (n), (v)] shows a plane at 25% of the channel depth apart from the top, and the third [Fig. 3(g), (o), (w)], 50% (symmetric plane), and the fourth [Fig. 3(h), (p), (x)], 75%. The locations for five cross-sectional images (the *XY*-plane) in the first column [Fig. 3(a–e), (i–m), (q–u)] were indicated by the lines in the second column. Each inset in the third column is a side view (the *YZ*-plane) of the location indicated by the line right below where the effect of the primary flow caused by −1.5° tilting with respect to the *X*-axis vanishes (see the Methods section). The curvature ratio *W/R* varied periodically with large amplitude (from −35 to 35%) along the streamwise direction where *R* is the radius of curvature. The maximum Dean number for each row is 6.53, 13.07, and 19.6, respectively. The Dean number is defined by $Dn = Re\sqrt{(W/R)}$.

As shown in the insets in Fig. 3(g), (o), and (w), the measured velocity field presented a pair of counter-rotating vortices (Dean cells), one in the upper half and the other in the lower half, as indicated above the inset in Fig. 3(o). The inset in Fig. 3(o) is divided into four areas which are separated by the black color, *i.e.* $v_y = 0$. Each area has circular color patterns. The outermost color in an area indicates the direction of v_y across the area. For example, the outermost color in the upper left area is blue which means that the direction of v_y is upward (negative v_y). The red color at the center of the upper left area does not mean positive v_y but more negative v_y because there is an abrupt color change from blue to red. A strong negative velocity caused an aliasing effect or a phase wrapping. Finally, we did the same analysis with changing the relative orientation between the incident light and the microchannel to verify the structure of the Dean cells. The centrifugal force exerted at each fluid element generated the vortices. Hence, the secondary flow moved from the inside to the outside side wall along the horizontal symmetric line. Since the curvature was alternating, the rotational direction of the vortices was also alternating, as shown by comparing Fig. 3(i) to (m). The first order of Dean's solution[12,13] for secondary flow velocity in a circular tube states that the maximum velocity component normal to the interface of the Dean cells is $(0.0096Dn^2/Re)V$ when $Dn < 24$. The measured values in the present study showed good agreement with it. It is shown in Fig. 3(b–d), (j–l), and (r–t) that the secondary flow was developing because of alternating curvature. The length required for full development increased with increasing flow rate, as indicated by the three lines in the middle of Fig. 3(f), (n), and (v). As mentioned before, Fig. 3(g), (o), and (w) depict the *y*-component of the velocity field in the symmetric plane. In this symmetric plane, the effect of the primary flow dominates because the secondary flow is almost normal to the incident light [at the positions, for instance, marked by in Fig. 2(b), the secondary flow is exactly normal to the incident light] and its magnitude is much smaller than the primary flow. The primary velocity profile deviated from the Poiseuille flow and the location, where maximum velocity is, moved from the center toward the outside side wall.

The second experiment was conducted to visualize the mixing pattern, as shown in Fig. 4. The same image-producing method as the first experiment was used. The Reynolds number for each row in Figs. (a–h) and (i–p) is 11 and 33, the Dean number is 6.53 and 19.6, and the Péclet number $Pe = VW/D$ is 1.26×10^7 and 3.79×10^7, respectively, where *D* is the molecular

diffusivity. The Pe´clet number is the ratio of convection to molecular diffusion. Convection dominates mixing phenomena in this condition. The mixing patterns in each row were imaged at the location labeled by the marks in Fig. 3(h) and (x). The mixing patterns were aligned to have the same direction of the primary flow [the label locations in Fig. 3(h) and (x) correspond to the left side of the mixing patterns in Fig. 4]. The different colors of the figure frames denote different curvature.

It is clearly shown that vertical interfaces [Fig. 4(a) and (i)] at the confluence were distorted and evolved by the counter-rotating vortices with alternating rotation. For instance, the interface intersecting with the symmetric plane moved back and forth. When comparing Fig. 4(d) with (f), the interface located at the center of the channel proceeded to the outer channel wall [indicated by the arrow in Fig. 4(f)] by 25% of the channel width. The proceeded distance calculated with the first order of Dean's solution is 20.8%. A movie clip for the volume-rendered mixing pattern is shown in Video 1 in the ESI[†] (Re = 11). Even though the secondary flow is exactly reversed when the curvature is reversed, the interface intersecting with the symmetric plane does not oscillate around the channel center. It is supposed that the biased oscillation is caused by the initial condition imposed before the first turn. When one sees the mixing from the top over the channel, it looks as if the two liquids are completely mixed. Alternately curving a channel, however, was not enough to make a complete mixing even at the end of the channel.

The third and fourth experiments were designed to enhance two-liquid mixing and to visualize the enhancement mechanism. The hypothesis was that injecting air into two liquids enhances mixing. By injecting air, a bubble-train flow[30–32] was sustained in a quasi-steady-state. Through the third experiment, the velocity field, which governs a mixing phenomenon, was imaged. The velocity field of bubble-train flow in the meandering microchannel is characterized by the Dean number Dn_j based on the overall superficial velocity j [= $(Q_l + Q_g)/A$] and the capillary number Ca. Those are defined as $Dn_j = jW/\nu\sqrt{(W/R)}$ and $Ca = \mu U_b/\sigma$, respectively, where Q_l and Q_g are the liquid and gas flow rates, respectively, A is the cross-sectional area, μ is liquid viscosity, σ is interfacial tension, and U_b is bubble velocity. The bubble velocity U_b and, therefore, Ca can be estimated from the overall superficial velocity.[31] The Dean number and the capillary number were about 5.4 and 2.7×10^{-4}, respectively, under the present experimental conditions. Since the flow has rapid, transient phenomena and the camera frame rate ($1/T$) is limited, it was impossible to acquire an instantaneous volume image. Therefore, the probe beam of SDDOCT was fixed at the locations indicated by the blue and red dots in Fig. 2(b) without **B**- and C-scans. Continuous camera exposure constitutes depth *versus* time images like in Fig. 5. The three blue dots, which are indicated by the numbers 1–3 in Fig. 2(b), evenly divide the channel width into quarters. Fig. 5(b–d) were taken at the lower, center, and upper blue dots, respectively. The red dot indicated by the number 4 is located 20 μm away from the outside side wall where Fig. 5(e) was taken.

In the liquid region far from the bubbles in Fig. 5(b–d), the secondary flow caused by the curvature was also observed. The maximum primary liquid velocity around the center of the cross-section far from the bubbles is about 1.8 times higher[31,32] than the bubble velocity with a capillary number of 2.7×10^{-4}. Therefore, a toroidal vortex per liquid slug was generated before and after the bubbles and made a longitudinal recirculation flow when this flow was seen in a coordinate system moving with the bubbles. The longitudinal recirculation adds a complexity to the transversal recirculation by the secondary flow to be the key mechanism for mixing enhancement. Fig. 5(a) is a schematic diagram for the three-dimensional flow field

[†]Electronic supplementary information (ESI) available: Theory of SDDOCT, supplementary video 1 (volume-rendered mixing pattern), 2 (enhanced mixing pattern 1 in bubble-train flow), 3 (enhanced mixing pattern 2 in bubble-train flow), and 4 (enhanced mixing pattern 3 in bubble-train flow). See DOI: 10.1039/b713626a

which gives rise to the mixing enhancement. Strong vertical (along the *y*-axis) liquid motions resulting from the toroidal vortices were detected as shown in Fig. 5(b–d). On the other hand, there is a bypass liquid flow at the corners of the square channel from the front liquid slug to the back because the cross-sectional average of primary liquid velocity is about 0.8 of bubble velocity.[31,32] The bypass flow is imaged in Fig. 5(e) with the longitudinal recirculation flow and can be observed only at the corners in this capillary number regime.

In order to visualize the enhanced mixing, the unmixed and vertically arranged two liquids were pumped into inlet 1 using the configuration A shown in Fig. 2(b). At the same blue dots, depth *versus* time images were recorded with the same gas and liquid flow rates and are shown in Fig. 6. The Péclet number Pe_j based on the overall superficial velocity was 1.04×10^7 in this condition. At a liquid slug far from the bubbles, the primary velocity profile made fluid elements disperse parabolically and this axial dispersion was perturbed by the alternating secondary dispersion shown in Fig. 4. In addition, longitudinal recirculation enhanced radial mixing near the bubbles. This transient mixing was also imaged at the 16 cross-sections along the lines of interest in Fig. 2(b). The transient mixing patterns at the 5th, 6th, 11th, 12th, 15th, and 16th cross-sections are presented in Fig. 7 and Videos 2–4 in the ESI† to compare with Fig. 4. Mixing performance was greatly enhanced. It was supposed that a complete mixing was done by the 15th cross-section with the current resolution limit (6.3 μm). As a matter of fact, the thickness of liquid layers (approx. initial thickness $\times 0.5^{\log Pe}$, where log *Pe* is the number of folding for a complete mixing) can be as small as a micron right before a complete mixing occurs when the Péclet number is high. If we have a ultra broadband light source with a shorter center wavelength, a submicron imaging is possible with SDDOCT. It is nevertheless difficult to measure concentration variation over a cross-section in order to determine a mixing uniformity.

The characteristic time for the longitudinal recirculation is defined as the time for the liquid to move from one end of the liquid slug to the other end. With the current capillary number, the longitudinal recirculation time is $3l_{ls}/U_b$ where l_{ls} is the length of the liquid slug.[32] The characteristic time for the alternating secondary flow is defined as the time for the liquid slug to go through one period of the meandering microchannel, l_p/U_b where l_p is length of one period of the microchannel. Therefore, $3l_{ls}/l_p$ means how many perturbations one can expect during the time for the liquid to move from one end of the liquid slug to the other end. In other words, $l_p/3l_{ls}$ means how many foldings by longitudinal recirculation one can expect during the time for the liquid slug to turn a period of the meandering microchannel. In the case of Fig. 6(b), the number $l_p/3l_{ls}$ was 1.18 and the total number of folding for the entire channel was about 8 which is almost equal to the number of folding for a complete mixing, log Pe_j.

The performance of two-liquid mixing is sensitive to arrangements of two liquids at the inlet. If the interface between the two liquids is oriented horizontally at inlet 1 using the configuration B shown in Fig. 2(b), the mixing will not be efficient because the perturbation caused by the alternating Dean cells will be of no use.

Conclusions

We applied SDDOCT to the visualization of secondary flow and two-liquid mixing inside a meandering microchannel in order to emphasize SDDOCT's uniqueness: out-of-plane velocity measurement and real-time, high-resolution cross-sectional imaging. We derived mathematical details about how the structural and velocity images were recorded simultaneously. Particularly, the Doppler effect was rigorously formulated in the context of SDDOCT for the first time. The Dean cells were quantified and compared to the analytical result. We imaged alternating Dean cells which served as periodic perturbation. A bubble injection method to

enhance the two-liquid mixing was proposed. The full enhancement mechanism was identified in three-dimensional space: alternating Dean cells and toroidal vortices.

As applications of lab-on-a-chip become more diverse, the geometry of the chip becomes more complex and the flow field inside the chip has been changed from a simple Poiseuille flow to three-dimensional fields. The complex nature of the chip requires a novel probe that acts like the scanning electron microscope in the semiconductor industry and assures quality control by diagnosing structure and flow in real-time and non-invasively. SDDOCT will be a strong candidate for the novel probe.

Acknowledgments

The authors acknowledge the support of the National Institutes of Health (EB-00293, NCI-91717, RR-01192), and the Air Force Office of Scientific Research (FA9550-04-1-0101). Institutional support from the Beckman Laser Institute Endowment is also gratefully acknowledged.

References

1. Ottino JM. Annu. Rev. Fluid Mech 1990;22:207.
2. Leitgeb RA, Schmetterer L, Drexler W, Fercher AF, Zawadzki RJ, Bajraszewski T. Opt. Express 2003;11:3116. [PubMed: 19471434]
3. Wang L, Wang Y, Guo S, Zhang J, Bachman M, Li GP, Chen Z. Opt. Commun 2004;242:345.
4. Ahn Y-C, Jung W, Chen Z. Appl. Phys. Lett 2006;89:064109.
5. Stroock AD, Dertinger SKW, Ajdari A, Mezic I, Stone HA, Whitesides GM. Science 2002;295:647. [PubMed: 11809963]
6. Pereira F, Gharib M. Meas. Sci. Technol 2002;13:683.
7. Ahn Y-C, Jung W, Chen Z. Opt. Lett 2007;32:1587. [PubMed: 17546197]
8. Knapik DA, Starkoski B, Pavlin CJ, Foster FS. IEEE Trans. Ultrason. Ferroelectr. Freq. Control 2000;47:1540. [PubMed: 18238700]
9. Kim GB, Lee SJ. Exp. Fluids 2006;41:195.
10. Kinney JH, Nichols MC. Annu. Rev. Mater. Sci 1992;22:121.
11. Eustice J. Proc. R. Soc. London, Ser. A 1910;84:107.
12. Dean WR. Philos. Mag 1927;4:208.
13. Dean WR. Philos. Mag 1928;5:673.
14. Berger SA, Talbot L, Yao L-S. Annu. Rev. Fluid Mech 1983;15:461.
15. Cheng KC, Lin R-C, Ou J-W. J. Fluids Eng 1976;98:41.
16. Ghia KN, Sokhey JS. J. Fluids Eng 1976;99:640.
17. Schönfeld F, Hardt S. AIChE J 2004;50:771.
18. Jiang F, Drese KS, Hardt S, Küpper M, Schönfeld F. AIChE J 2004;50:2297.
19. Back LH, Cho YI, Crawford DW, Blankenhorn DH. J. Biomech. Eng 1987;109:90. [PubMed: 3560886]
20. Back LH, Kwack EY, Crawford DW. J. Biomech. Eng 1988;110:310. [PubMed: 3205016]
21. Agrawal Y, Talbot L, Gong K. J. Fluid Mech 1978;85:497.
22. Talbot L, Gong KO. J. Fluid Mech 1983;127:1.
23. Eustice J. Proc. R. Soc. London, Ser. A 1911;85:119.
24. Akiyama, M.; Hanaoka, Y.; Cheng, KC.; Urai, I.; Suzuki, M. Flow visualization III. Yang, WJ., editor. Washington: Hemisphere Pub. Corp; 1985. p. 526-530.
25. Song H, Bringer MR, Tice JD, Gerdts CJ, Ismagilov RF. Appl. Phys. Lett 2003;83:4664. [PubMed: 17940580]
26. Hausler G, Lindner MW. J. Biomed. Opt 1998;3:21.
27. Tomlins PH, Wang RK. J. Phys. D: Appl. Phys 2005;38:2519.
28. Yun SH, Tearney GJ, de Boer JF, Bouma BE. Opt. Express 2004;12:2977. [PubMed: 19483816]

29. Zhao Y, Brecke KM, Ren H, Ding Z, Nelson JS, Chen Z. IEEE J. Sel. Top. Quantum Electron 2001;7:931.

30. Gunther A, Khan SA, Thalmann M, Trachsel F, Jensen KF. Lab Chip 2004;4:278. [PubMed: 15269792]

31. Thulasidas TC, Abraham MA, Cerro RL. Chem. Eng. Sci 1995;50:183.

32. Thulasidas TC, Abraham MA, Cerro RL. Chem. Eng. Sci 1997;52:2947.

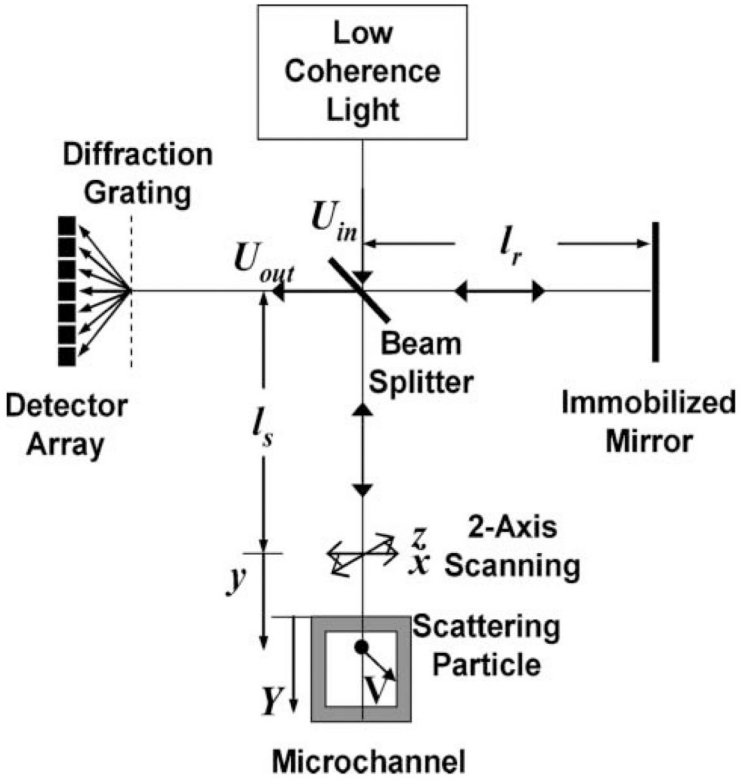

Fig. 1.
Michelson interferometer for spectral-domain Doppler optical coherence tomography.

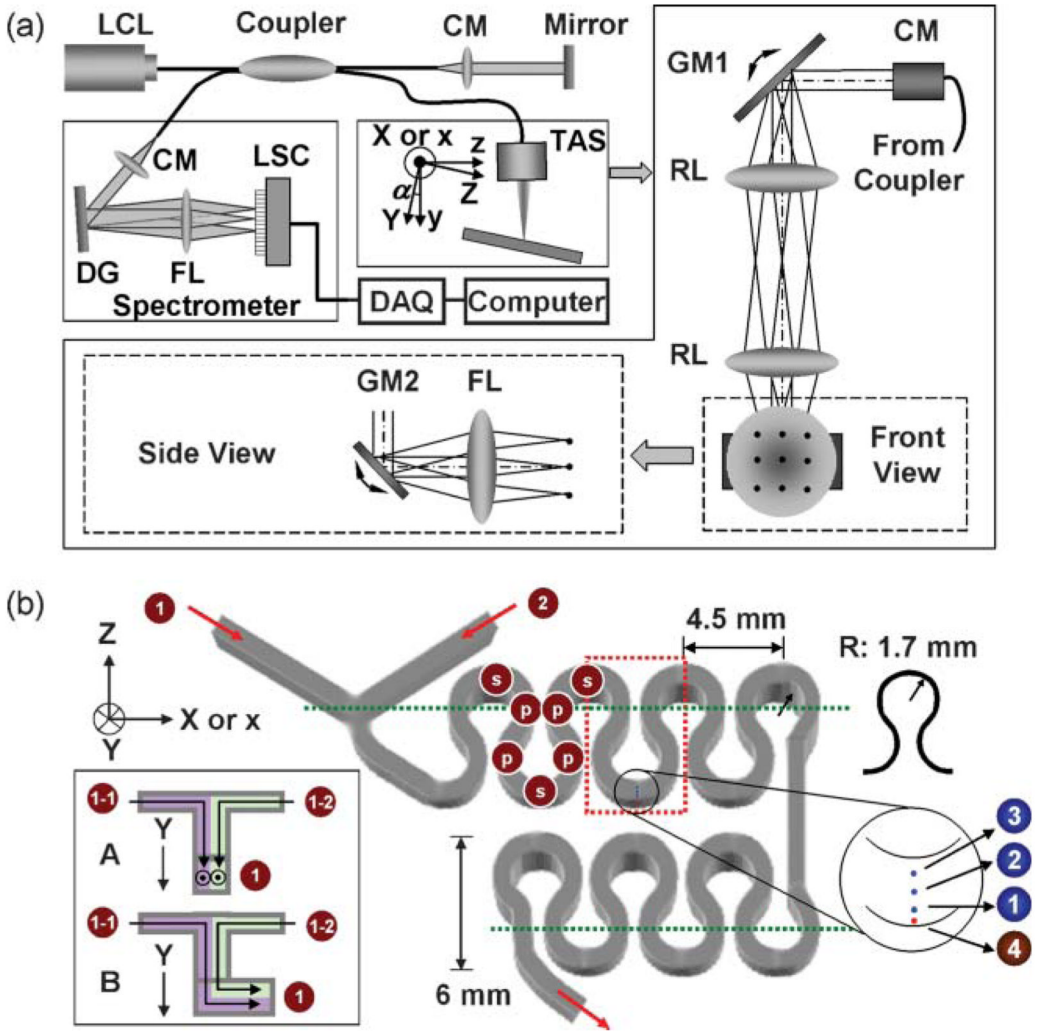

Fig. 2.

Experimental setup. (a) Schematic diagram for spectral-domain Doppler optical coherence tomography, and (b) a meandering square microchannel: (-----) area of interest; (-----) line of interest; (· or ·) point of interest; LCL: low-coherence light; CM: collimator; DG: diffraction grating; FL: focusing lens; LSC: line scan camera; GM: galvo mirror; RL: relay lens, TAS: two-axis scanner.

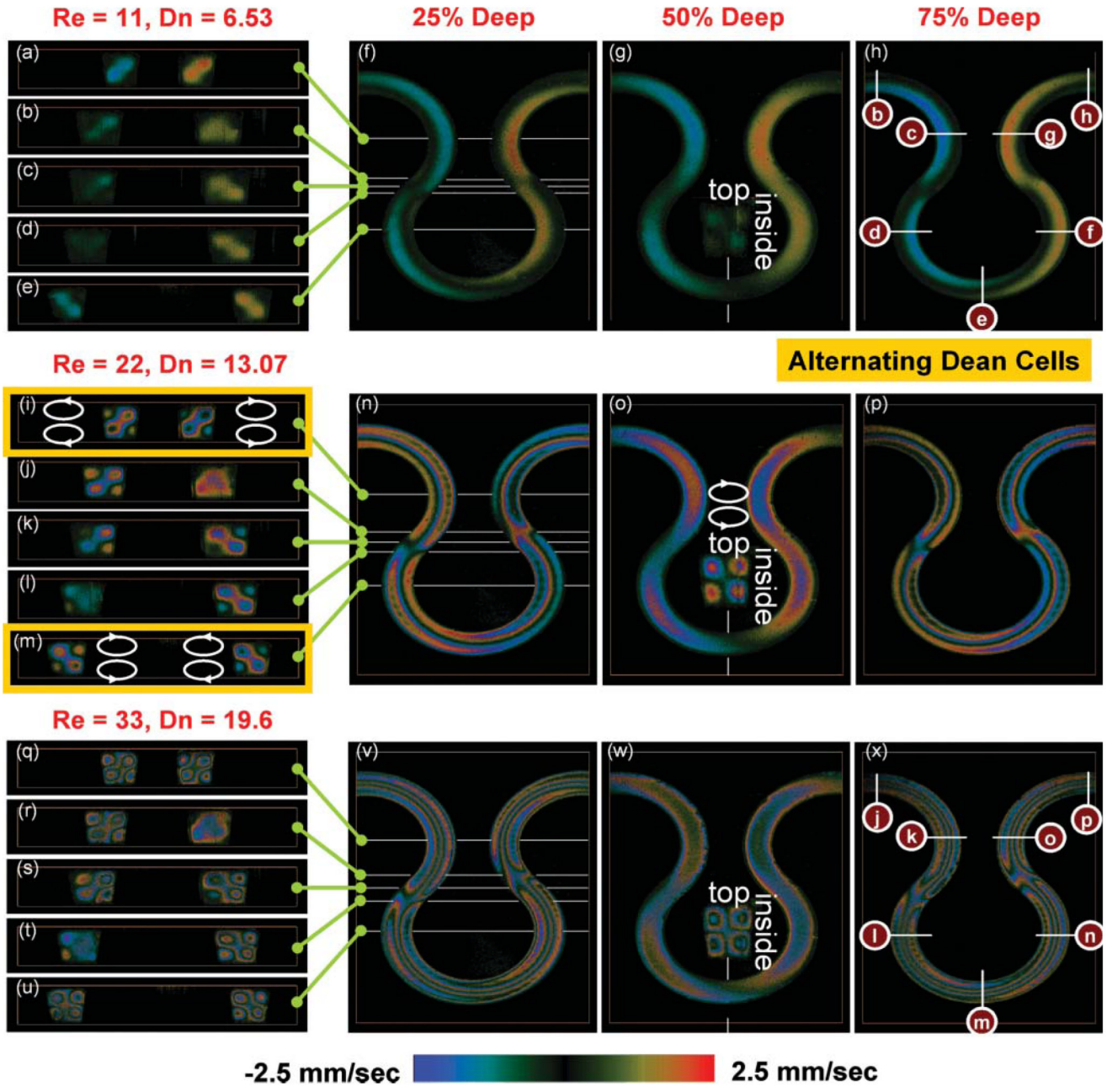

Fig. 3.

The liquid velocity $v_y(X, Y, Z)$ projected on the incident light in the area of interest. The velocity field shows a pair of counter-rotating vortices indicated above the inset in (o). Since the curvature is alternating, the rotational direction of the vortices is also alternating as shown by comparing (i) to (m). (a–e, i–m, q–u) The *y*-component velocity field $v_y(X, Y, Z)$ sectioned by the *XY*-planes. (f–h, n–p, v–x) The *y*-component velocity field $v_y(X, Y, Z)$ sectioned by the *XZ*-planes. (Insets in g, o, w) The *y*-component velocity field $v_y(X, Y, Z)$ sectioned by the *YZ*-planes.

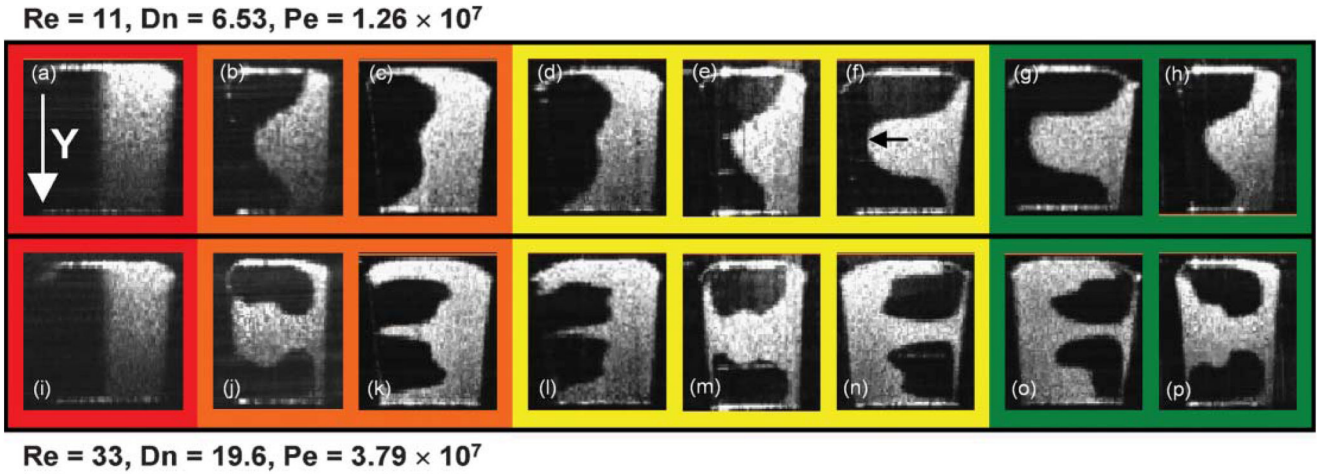

Fig. 4.

Cross-sectional mixing pattern of water and polystyrene suspension is evolving and oscillating along the meandering channel. The oscillating is caused by the secondary flow. When one sees the mixing from the top over the channel, it looks as if two liquids were completely mixed. Alternately curving a channel, however, is not enough to make a complete mixing. Each horizontal row has a different flow rate.

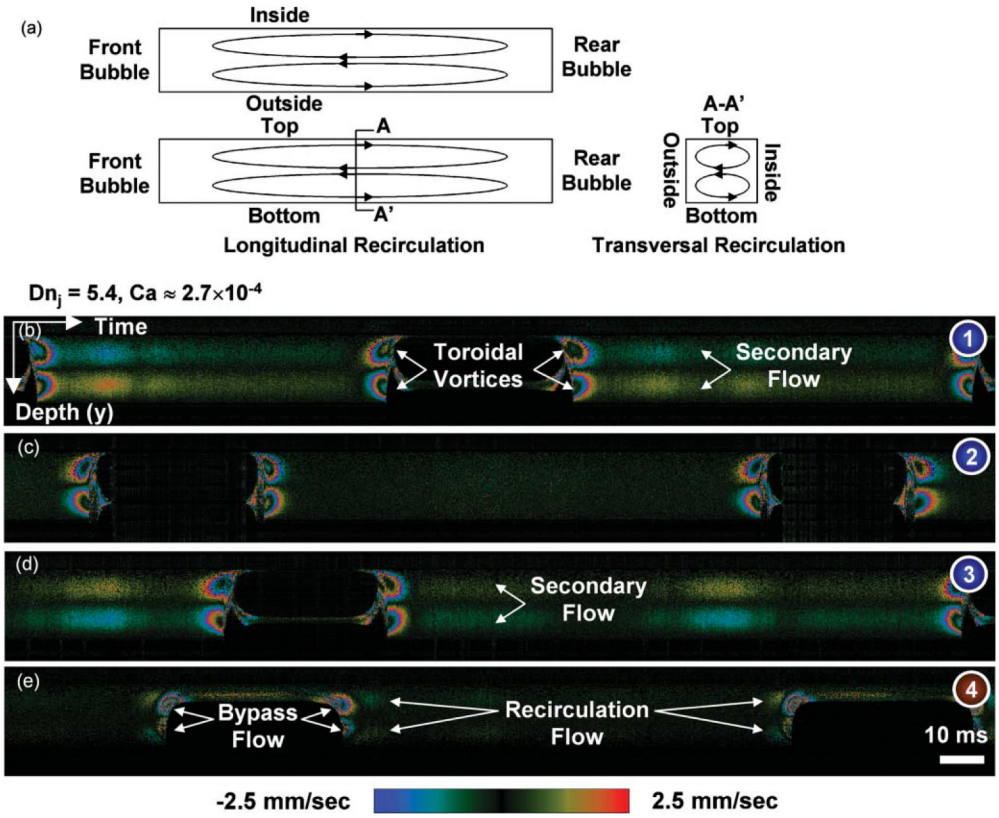

Fig. 5.

Depth *versus* time images showing liquid velocities projected on the incident light $v_y(y, t)$. (a) Schematic diagram illustrating the three-dimensional flow field which gives rise to mixing enhancement. (b–d) Liquid slug in bubble-train that flows through a meandering microchannel has not only a transversal recirculation by the secondary flow but also a longitudinal recirculation associated with the toroidal vortices to enhance mixing performance. (e) A bypass flow with the longitudinal recirculation imaged. Each image was taken at a different point of interest shown in Fig. 2(b).

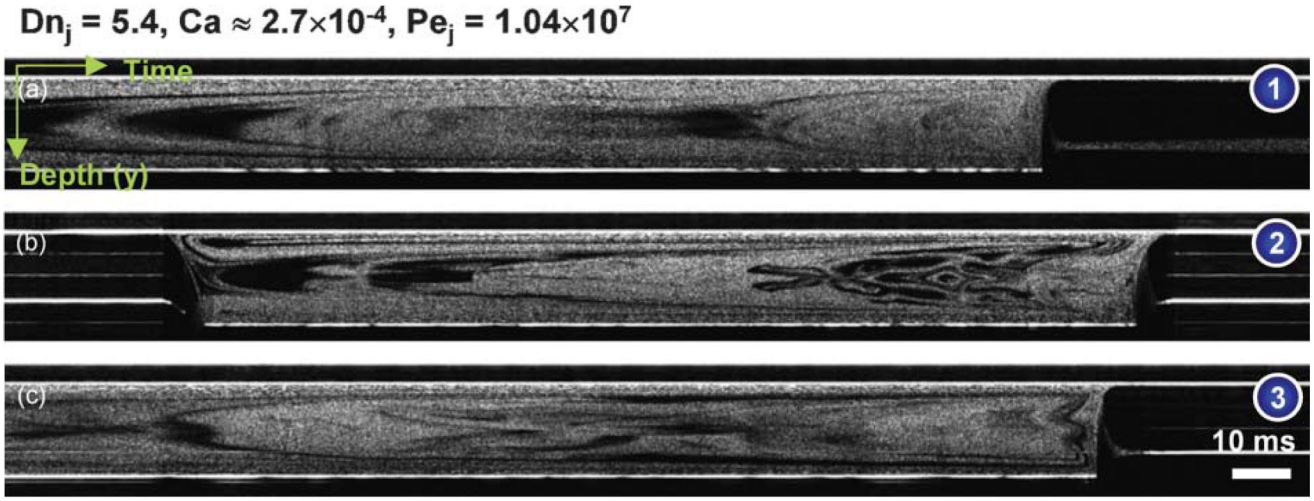

Fig. 6.

Depth *versus* time images showing an enhanced mixing pattern of water and polystyrene suspension within a liquid slug of bubble-train flow. Each image was taken at a different point of interest shown in Fig. 2(b).

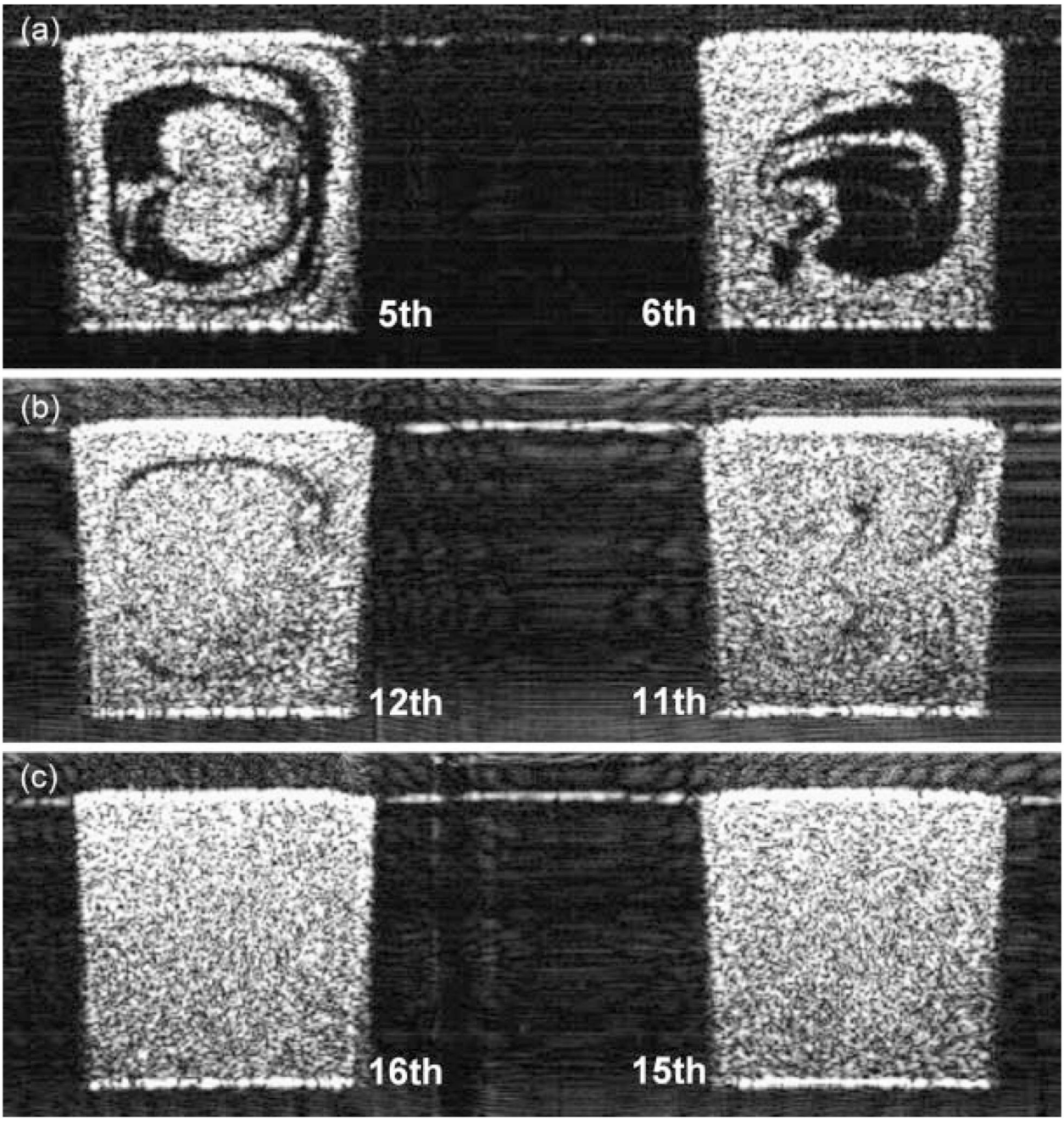

Fig. 7.

Transient mixing patterns enhanced by the bubble-train flow were imaged at the 5th, 6th, 11th, 12th, 15th, and 16th cross-sections (see Videos 2–4 in the ESI[†]). It was supposed that a complete mixing was done by the 15th cross-section with the current resolution limit of 6.3 μm. $Dn_j = 5.4$, $Ca \approx 2.7 \times 10^{-4}$, $Pe_j = 1.04 \times 10^7$.

Table 1

Comparison of techniques for microscale visualization

Modalities	Available techniques	Spatial dimension	Spatial resolution/ μm	Imaging depth/mm	Frame rate for 2D slice	Simultaneous measurement of flow and mixing	Number of Velocity components	Cost	Features
Fluorescence microscopy	μPIV[a]	2D	5	N/A	Slow	No	2 or 3	Low	Non-invasive
	FR- or PR-based[b]		1		Real time				
Confocal aser Scanning microscopy	μPIV FR- or PR-based	2D or 3D	5 1	0.5	Slow Real time	No	2	High	Non-invasive
OCT	Doppler OCT	2D or 3D	2–10	2–3	Real time	Yes	1 or 3	Low	Non-invasive, turbid liquids
Ultrasound	Echo PIV[c]	2D	400	16	Slow	No	2	High	Contact, opaque conduits
	Ultrasound biomicroscopy[d]	2D or 3D	15	0.6	Real time	Yes	1		
X-Ray	μPIV[e]	2D	13	N/A	Slow	No	2	Very high	Non-invasive opaque conduits
	Industrial CT	2D or 3D	50–100	Unlimited					
	X-Ray tomography microscopy[e]	2D or 3D	2–3	10					

[a] μPIV: micro particle imaging velocimetry.

[b] FR: fluorescence; PR: phosphorescence.

[c] With 7.8 MHz frequency.

[d] With 200 MHz frequency.

[e] With synchrotron X-ray source.

Table 2

Experimental conditions

	Expt 1		**Expt 2**		**Expt 3**		**Expt 4**		
Inlet port	1	2	1	2	1	2	1–1[a]	1–2[a]	2
Fluid[b]	W/P	W/P	W	W/P	W/P	A	W/P	W	A
Flow rate/	0.2	0.2	0.2	0.2	0.25	0.08	0.125	0.125	0.08
ml min^{-1}	0.4	0.4	0.6	0.6					
	0.6	0.6							

[a] With the configuration A as shown in Fig. 2(b).

[b] W/P: water with particle (2.5% aqueous suspension of polystyrene beads); W: water; and A: air.

Lab Chip. Author manuscript; available in PMC 2010 May 12.